

1       **High-accuracy  $^{12}\text{C}^{16}\text{O}_2$  line intensities in the 2  $\mu\text{m}$  wavelength region measured by**  
2                               **frequency-stabilized cavity ring-down spectroscopy**

3  
4       Hongming Yi, Qingnan Liu, Lyn Gameson, Adam J. Fleisher\* and Joseph T. Hodges

5                               *National Institute of Standards and Technology*

6                               *100 Bureau Drive, Gaithersburg, Maryland 20899, U.S.A.*

7                               December 11, 2017

8                               Corresponding author: [adam.fleisher@nist.gov](mailto:adam.fleisher@nist.gov)

9  
10   **ABSTRACT:** Reported here are highly accurate, experimentally measured ro-vibrational  
11 transition intensities for the R-branch of the (20012) - (00001)  $^{12}\text{C}^{16}\text{O}_2$  band near  $\lambda = 2 \mu\text{m}$ .  
12 Measurements were performed by a frequency-stabilized cavity ring-down spectroscopy (FS-  
13 CRDS) instrument designed to achieve precision molecular spectroscopy in this important region  
14 of the infrared. Through careful control and traceable characterization of  $\text{CO}_2$  sample conditions,  
15 and through high-fidelity measurements spanning several months in time, we achieve relative  
16 standard uncertainties for the reported transition intensities between 0.15 % and 0.46 %. Such high  
17 accuracy spectroscopy is shown to provide a stringent test of calculated potential energy and *ab*-  
18 *initio* dipole moment surfaces, and therefore transition intensities calculated from first principles.

19  
20  
21   **KEYWORDS:** Precision molecular spectroscopy, line lists, carbon dioxide, cavity ring-down  
22 spectroscopy, infrared spectroscopy, dipole moment surfaces

## 24 **1 Introduction**

25 The remote sensing of atmospheric molecules relies upon first-principles, physics-based  
26 models that incorporate accurate and precise laboratory spectroscopic data. For example, current  
27 satellite-based measurements of atmospheric CO<sub>2</sub>, such as the ongoing GOSAT (JAXA), and  
28 OCO-2 (NASA) missions and the upcoming MICROCARB (CNES) mission, as well as the  
29 worldwide terrestrial spectrometer campaign (TCCON), demand low uncertainty in the pressure,  
30 temperature and composition dependence of air-broadened O<sub>2</sub> and CO<sub>2</sub> absorption cross sections.  
31 These quantities can be calculated in terms of absolute transition frequencies and intensities, and  
32 line shape parameters that account for collisional broadening, pressure shifting, line mixing and  
33 collisional narrowing [1, 2]. In the context of NASA's Earth-orbiting OCO-2 satellite mission  
34 which measures the column-integrated dry air mixing ratio of CO<sub>2</sub> [3], calculated cross-sections  
35 with relative uncertainties on the order of 0.3 % are required [4]. In order to meet this ambitious  
36 data target and therefore maximize the scientific achievements of this and other remote-sensing  
37 missions, reference-quality, laboratory measurements of CO<sub>2</sub> spectroscopic parameters are  
38 required.

39 Here we report a detailed description of the instrumentation and methodology used to  
40 perform low-uncertainty cavity ring-down spectroscopy (CRDS) measurements of relatively  
41 strong carbon dioxide line intensities in the wave number region 4 990 cm<sup>-1</sup> to 5 010 cm<sup>-1</sup>. The  
42 resulting intensities are reproduced with high fidelity over a period of several months with relative  
43 combined standard uncertainties of 0.25 %. Comprehensive comparisons with existing database  
44 parameters as well as recent *ab initio* and experimental intensities are reported and discussed.

45  
46

## 47 **2 Description of Experiment**

### 48 *2.1 Survey of spectral region*

49 The upper panel of Fig. 1 shows a simulated air-broadened absorption spectrum of carbon  
50 dioxide (with water vapor interferences) for the wave number region investigated here and for  
51 pressure, moisture, mole fraction and path length conditions representative of this study. The  
52 spectrum is dominated by 19 targeted transitions assigned to the (20012) - (00001) vibrational  
53 band of <sup>12</sup>C<sup>16</sup>O<sub>2</sub> lower-state rotational quantum numbers  $J'' = 16, 18, \dots 52$ . The lower panel of  
54 Fig. 1 has the same calculated spectrum plotted with a logarithmic ordinate, showing that the

55 interferences associated with other  $^{12}\text{C}^{16}\text{O}_2$ ,  $^{13}\text{C}^{16}\text{O}_2$  and  $\text{H}_2\text{O}$  transitions are typically at most two  
56 orders of magnitude below the peak absorption of the target transitions. Although, the targeted  
57 transitions were relatively isolated, because of the high signal-to-noise ratio of the measured  
58 spectra, our analyses accounted for the wings of neighboring strong lines as well as residual  
59 contributions from some of the weak interferences.

60

## 61 2.2 *FS-CRDS method*

62 We acquired absorption spectra using the frequency-stabilized cavity ring-down  
63 spectroscopy (FS-CRDS) method. This is an implementation of CRDS in which the optical  
64 resonator (i.e. ring-down cavity) is length-stabilized relative to a continuous-wave (CW),  
65 frequency-stabilized reference laser and pumped by a narrow line width CW probe laser [5, 6].  
66 FS-CRDS results in high-fidelity spectra that are determined from precise measurements of optical  
67 frequency shifts and intensity decay times. The active locking scheme in FS-CRDS ensures that  
68 the cavity mode spacing provides a stable and linear frequency detuning axis, and the single-mode  
69 excitation of the resonator eliminates laser bandwidth effects that can lead to complicated multi-  
70 exponential decay signals [7]. At each frequency step, the probe laser beam is brought into  
71 resonance with a single cavity mode (designated by its mode order  $q$ ) and subsequently switched  
72 off to cause single-exponential decay of the light intensity exiting the resonator. In this fashion,  
73 the spectrum detuning relative to the first mode order  $q_0$  is equal to  $(q - q_0)\nu_f = \Delta q\nu_f$  where  $\nu_f$   
74 is the cavity free spectral range (FSR). Individual intensity decay signals are converted into  
75 photocurrent with a DC-coupled photodetector, amplified and recorded using a high-speed A/D  
76 board. The time constant  $\tau$  for each decay event is obtained by fitting the three-parameter function  
77  $s(t) = Ae^{-t/\tau} + s_0$  to the time-dependent photocurrent signal  $s(t)$ , where  $A$  and  $s_0$  are the  
78 amplitude and time-independent offset, respectively. Multiple decays are obtained at each  
79 frequency detuning to provide an average decay time  $\bar{\tau}$  and standard deviation  $\sigma_\tau$ . Measured  
80 spectra are given by the set of values  $\alpha_{tot}(\Delta q\nu_f) = (c\bar{\tau})^{-1}$  where  $c$  is the speed of light. These data  
81 quantify the total (i.e. absorption plus baseline) intensity loss-per-unit length in the sample as a  
82 function of spectrum detuning.

83

84 2.3 *FS-CRDS spectrometer*

85 The FS-CRDS spectrometer used in this study is similar to other systems that were  
86 developed at the National Institute of Standards and Technology (NIST) in Gaithersburg, MD [8-  
87 10]. This spectrometer comprises several component sub-systems, including a high-finesse optical  
88 resonator and gas cell, a reference laser and servo controller for active resonator length  
89 stabilization, gravimetrically prepared gas mixtures of CO<sub>2</sub> in N<sub>2</sub> and associated flow delivery  
90 system, a tunable CW probe laser, a photoreceiver and digitizer, and a personal computer with  
91 high-speed data acquisition, signal analysis and control software. Each instrument sub-system is  
92 discussed in detail in this Section.

93 The optical instrument is assembled on a 1 m by 1.3 m breadboard seated atop a mobile  
94 cart. A standard rack mount, also on wheels, houses the fiber laser amplifier, oscilloscope, power  
95 supplies, locking and system control electronics, and a personal computer. An additional rack  
96 mount is situated next to the optical table with a gas cylinder mount and flow delivery manifold.

97  
98 2.4 *Optical resonator and gas cell*

99 The optical resonator and gas cell consist of two flexure mirror mounts supported by  
100 individual steel brackets, four 2.54 cm diameter invar rods 52 cm in length connecting the brackets,  
101 and a 1.27 cm diameter tube with formed bellows to connect the two mirror mounts and house the  
102 gas sample and optical cavity [5]. As shown in Fig. 2, each flexure mirror mount has a gas inlet  
103 (outlet) port used to exchange sample gas in a flowing configuration (see Section 2.5), with the  
104 gas sweeping past both ring-down mirrors to prevent the occurrence of dead volumes. Commercial  
105 dual-wavelength-coated, high-reflectivity low-loss mirrors (2.54 cm diameter, 6 m radius of  
106 curvature) with intensity reflection coefficients of 0.99964 and 0.95 at  $\lambda = 2 \mu\text{m}$  and  $\lambda = 633 \text{ nm}$ ,  
107 respectively, are installed into each flexure mount. The distance between the ring-down cavity  
108 mirrors is nominally 75 cm and accurately determined by measurement of the cavity FSR as  
109 discussed below. The vacuum seal between the intra-cavity gas sample and the laboratory  
110 environment is made by anti-reflection-coated CaF<sub>2</sub> windows which are bonded to a standard  
111 knife-edge-seal flange. This design results in the low-loss, ring-down cavity mirrors experiencing  
112 zero pressure difference between their high-reflection and anti-reflection coated faces, thus  
113 mitigating potential stress-induced birefringence effects [11, 12].

114 The FSR of the evacuated optical cavity was measured using an infrared wavelength meter  
115 (1  $\mu\text{m}$  to 5  $\mu\text{m}$  operating wavelength range) with a frequency resolution of 40 MHz. While a  
116 software-based dither locking scheme [13] maintained probe laser transmission, a small portion of  
117 the probe laser beam was analyzed by the wavelength meter for up to 12 s. The probe laser  
118 frequency was sequentially locked to 750 successive longitudinal modes of the optical resonator  
119 and the probe laser frequency was measured at each step. From these data, linear regression  
120 analysis yielded the empty-cavity free spectral range  $\nu_f = 200.806$  MHz with a standard  
121 uncertainty of 60 kHz. This value was in good agreement with  $\nu_f$  obtained by fitting a spectral  
122 model with known  $^{12}\text{C}^{16}\text{O}_2$  transition frequencies [14] to a measured absorption spectrum. Also,  
123 at each pressure and temperature condition, the  $\nu_f$  was corrected to account for density-dependent  
124 changes in the refractive index of the sample gas. These corrections were found to be less than  
125 0.02 % of the empty-cavity values for all conditions considered.

126

### 127 2.5 *Active length stabilization of optical resonator*

128 The mirror-to-mirror distance of the ring-down cavity was actively stabilized in order to  
129 provide a linear and stable relative frequency axis. To this end, a temperature-stabilized HeNe  
130 laser (100 kHz line width at 10 ms, long-term stability of 1 MHz), counter-propagating and co-  
131 linear with the probe laser, was simultaneously coupled to the optical resonator. A slow frequency  
132 dither was summed with a constant DC voltage and amplified to drive the free-space 633 nm  
133 acousto-optic modulator (AOM). The AOM was aligned in a double-pass configuration to  
134 minimize pointing changes associated with changes in frequency. A commercial photoreceiver  
135 measured the HeNe transmission as a function of the AOM dither waveform, and an error signal  
136 was generated using a lock-in amplifier. A servo controller was fed back to a cylindrical piezo-  
137 electric (PZT) actuator with 12  $\mu\text{m}$  of travel range. The PZT was attached to the output mirror of  
138 the optical resonator in order to enable precise control of the ring-down cavity mirror-to-mirror  
139 distance. Slow drifts in cavity length associated with laboratory temperature were mitigated by the  
140 low-expansion invar rods in the cavity construction. Additionally, an insulated enclosure was  
141 placed around the optical resonator/sample cell assembly to further dampen temperature  
142 fluctuations during long-term data acquisition. All data were acquired at room temperature  
143 conditions ( $298.3 \text{ K} \pm 1.3 \text{ K}$ ).

144

145 2.6 *Certified gas cylinders and flowing delivery system*

146 Two gas cylinders of dilute CO<sub>2</sub> in a balance of dry N<sub>2</sub> were certified against  
147 gravimetrically prepared standards by the Gas Sensing Metrology Group at NIST. The certified  
148 CO<sub>2</sub> (all isotopologues) molar fractions were  $\chi_{CO_2} = 49.826 \mu\text{mol/mol} \pm 0.019 \mu\text{mol/mol}$  (mixture  
149 A) and  $\chi_{CO_2} = 100.474 \mu\text{mol/mol} \pm 0.057 \mu\text{mol/mol}$  (mixture B), respectively (uncertainties are  
150 calculated with a coverage factor of  $k = 1$ ). Regulated flow from a chosen gas cylinder was throttled  
151 by a metering valve prior to entering the optical resonator via an inlet port located near the anti-  
152 reflection (AR) side of the input mirror. The sample gas flow rate and pressure could be adjusted  
153 to a range of conditions using a mass flow controller and diaphragm pump, respectively, located  
154 downstream of the optical cavity. Also, a proportional-integral controller located downstream of  
155 the optical resonator was used to maintain a constant gas pressure (less than 1.5 Pa variation) in  
156 the measurement volume. This arrangement used a high-precision capacitance diaphragm gauge  
157 and a solenoid-actuated flow needle valve to overcome pressure fluctuations caused by changes in  
158 pumping speed and upstream pressure. Experiments were performed on both certified gas  
159 cylinders at multiple steady-state pressures and at two distinct flow rates ( $10 \text{ cm}^3 \text{ min}^{-1}$  and  $20$   
160  $\text{cm}^3 \text{ min}^{-1}$ , respectively).

161

162 The relative isotopic composition  $\delta^{13}C_{VPDB} = \frac{^{13}C / ^{12}C}{[^{13}C / ^{12}C]_{ref}} - 1$  of both certified gas samples  
163 was determined here by Fourier-transform spectroscopy (FTS) measurements of  $^{12}C^{16}O_2$  (R10 and  
164 R18 transitions of the (10012) - (00001) band) and  $^{13}C^{16}O_2$  (P10, P14, and P22 transitions of the  
165 (00012) - (00001) band). The sample  $\delta^{13}C_{VPDB}$  values were determined by reference to a previously  
166 characterized CO<sub>2</sub> sample with a known value of  $\delta^{13}C_{VPDB}$ , where VPDB indicates the Vienna Pee  
167 Dee Bee scale defined to have a reference value of  $(^{13}C/^{12}C)_{ref, VPDB} = 0.011 237 2$ . For both  
168 certified gas samples, the FTS measurements performed at NIST gave  $\delta^{13}C_{VPDB} \approx -40 \text{ ‰}$  which  
169 is typical of carbon dioxide that is of petrochemical origin. Assuming  $\delta^{18}O_{VPDB} = -24 \text{ ‰}$  which is  
170 typical of petroleum-derived carbon dioxide and a stochastic distribution of C and O isotopes,  
171 yields a relative abundance of the  $^{12}C^{16}O_2$  (626) isotopologue equal to  $0.984 7 \pm 0.000 1$  for the  
172 both sample gases. We note that this value is approximately 0.05 % greater than the relative  
173 abundance  $\chi_{626,HT} = 0.984 2$  assumed in the HITRAN database. Following this convention, all

174 measured intensities reported below are normalized to a  $^{12}\text{C}^{16}\text{O}_2$  relative abundance corresponding  
175 to  $\chi_{626,HT}$  using the multiplicative factor  $\chi_{626,HT}/\chi_{626} = 0.999\,463$ .

176

### 177 2.7 *Measurement of sample temperature and pressure*

178 Temperature and pressure measurements were performed using NIST-calibrated sensors  
179 and instruments with traceability to the SI. Sample gas conditions corresponded to five pressures  
180 ranging from 6 kPa to 34 kPa. The temperature was measured by a 100  $\Omega$  industrial-grade,  
181 platinum resistance thermometer (PRT) located at the mid-plane of the resonator (20 mK Type B  
182 standard uncertainty) and in direct contact with the outside surface of the stainless steel tubing  
183 (OD = 1.25 cm) forming the ring-down cavity enclosure. The PRT temperature was logged  
184 continuously yielding an average standard deviation of 40 mK during the time to acquire each  
185 spectrum. Temperature uniformity was confirmed to be better than  $\Delta T < 30$  mK by making a series  
186 of Type-J thermocouple electromotive force measurements across the gas cell. The absolute  
187 pressure of the gas sample under flowing conditions was measured outside of the pressure control  
188 loop described in Section 2.6 by a resonant-Si gauge manometer with a full-scale range of 133  
189 kPa. This gauge was calibrated against a NIST pressure standard, resulting in Type B standard  
190 relative uncertainties between 0.004 % and 0.002 % over the entire measurement range. Further,  
191 the pressure difference across the gas cell under flowing conditions was measured to be  $< 0.008$  %  
192 of the mean value.

193

### 194 2.8 *Probe laser and optical detection*

195 Continuous spectral coverage from 4 989  $\text{cm}^{-1}$  to 5 009  $\text{cm}^{-1}$  was achieved by two fiber-  
196 coupled distributed feedback (DFB) laser diodes, each with a linewidth less than 2 MHz. An  
197 optical fiber amplifier increased the laser power to 20 mW before injection into an AOM operating  
198 at 55 MHz. The first-order output of this probe laser AOM was subsequently coupled into the  
199 optical resonator. Laser tuning and cavity resonance was achieved as described in [13], and cavity  
200 decays were initiated by switching off the RF power to the probe laser AOM.

201 Light decaying from the optical resonator was detected using a DC-coupled, photoreceiver  
202 comprising a liquid- $\text{N}_2$ -cooled 0.5-mm-diameter InSb photodiode and a transimpedance amplifier.  
203 The manufacturer's specifications included: photodiode responsivity of 1.45 A/W and noise-  
204 equivalent power (NEP) of 0.2  $\text{pW Hz}^{-1/2}$ ; amplifier bandwidth of 20 MHz and gain of  $2 \times 10^4$  V/A.

205 Triggered signal levels (1 V) corresponded to about 35  $\mu\text{W}$  of peak optical power. The  
 206 photoreceiver output signal was digitized by a 16-bit acquisition card (1  $\text{M}\Omega$  input impedance) at  
 207 a sampling rate of 200 MSamples/s. We measured integrated root-mean-square (RMS) noise levels  
 208 (DC-100 MHz) equal to 0.3 mV and 1.3 mV for the digitizer board and photoreceiver, respectively.  
 209 A detailed analysis of the noise power spectral density revealed non-white-noise behavior with a  
 210 much lower spectral density in the frequency range relevant to the decay time measurement (0.08  
 211 mV at 1 MHz bandwidth).

212 Decay signals were fit in real time using a fast fitting algorithm [15], and at each spectrum  
 213 detuning step 150 decay signals were averaged to provide  $\bar{\tau}$  and the ensemble standard deviation  
 214  $\sigma_{\tau}$ . For the empty-cavity case, the relative decay time measurement precision  $\sigma_{\tau}/\bar{\tau}$  and decay  
 215 signal acquisition rate were approximately 0.06 % and 10 Hz, respectively, corresponding to a  
 216 minimum noise-equivalent absorption coefficient (NEA) of  $10^{-9} \text{ cm}^{-1} \text{ Hz}^{-1/2}$ . Allan deviation  
 217 analysis of the decay time statistics resulted in a minimum detectable absorption coefficient of  
 218  $10^{-10} \text{ cm}^{-1}$  when averaging 1 000 measured decay events.

219 In order to address possible systematic effects associated with our choice of  
 220 detector/amplifier system, a limited number of spectra also were acquired with another detection  
 221 system: a thermoelectrically cooled, DC-coupled, InGaAs photodiode (0.3 mm diameter, 0.9 V/A)  
 222 coupled to a transimpedance amplifier ( $6.2 \times 10^4 \text{ V/A}$ ) with 10 MHz of bandwidth. The spectral  
 223 noise density of this system exhibited a relatively white frequency distribution, with integrated  
 224 values 3.5 to 2 times greater (over the ranges DC-100 kHz to DC-10 MHz, respectively) than those  
 225 observed with the InSb photoreceiver. Most importantly, compared to the InSb photoreceiver  
 226 system, the decay time measurement precision was degraded 7- to 10-fold.

227

228

### 229 3. Data Analysis

#### 230 3.1 Spectrum Model

231 All measured spectra (in dimensions of loss-per-unit length) were modeled as

$$232 \quad \frac{1}{c\bar{\tau}(\Delta\nu_q)} = \alpha_b(\Delta\nu_q) + \sum_{n=1}^n \alpha_n(\Delta\nu_q) \quad (1)$$

233 in which  $\Delta\nu_q = \Delta q\nu_f$  is the spectrum detuning,  $\alpha_b(\Delta\nu_q)$  represents the base cavity losses (mirror  
 234 reflectivity, scattering losses and etalons etc.) and  $\alpha_n(\Delta\nu_q)$  corresponds to the absorption

235 coefficient of the  $n^{\text{th}}$  observed molecular transition. For the limited spectral regions considered  
 236 here no etalons in the spectrum baseline were observed and it was sufficient to model  $\alpha_b(\Delta\nu_q)$  as  
 237 a linear function of  $\Delta\nu_q$ . The summation over  $n$  absorption transitions accounts for blended spectra  
 238 caused by spectral interferences such as those shown in Fig. 1, including both water vapor and  
 239 relatively weak CO<sub>2</sub> lines. The absorption coefficient from each line was modeled by

$$240 \quad \alpha_n(\Delta\nu_q) = A_n g_n(\nu_0 + \Delta\nu_q - \nu_n), \quad (2)$$

241 where  $A_n$  is the line area,  $g_n$  is the area-normalized line profile (described below),  $\nu_0$  is the  
 242 absolute frequency of the first spectrum point, and  $\nu_0 + \Delta\nu_q - \nu_n$  is the spectrum detuning relative  
 243 to transition  $n$  located at center frequency  $\nu_n$ .

244 In order to minimize uncertainty in determining the areas of the target transitions, we chose  
 245 to model these line shapes with the quadratic speed-dependent Nelkin-Ghatak line profile  
 246 (qSDNGP) [16]. No attempt was made to determine physically meaningful line profile parameters  
 247 from these data. This profile, also known as the quadratic speed dependent hard collision profile  
 248 (qSDHC), accounts for both collisional (Dicke) narrowing and speed dependent effects in the  
 249 quadratic approximation and is a limiting case of the recently recommended Hartmann-Tran  
 250 profile (HTP) [17]. In addition to the line area  $A_n$  and line center  $\nu_n$ , remaining parameters of the  
 251 qSDNGP include: Doppler half-width, velocity-averaged Lorentzian half-width, speed dependent  
 252 relaxation rate, velocity-averaged line shift, speed-dependent line shift, and frequency of velocity-  
 253 changing collisions given by  $(\Gamma_D, \Gamma_0, \Gamma_2, \Delta_0, \Delta_2, \nu_{vc})$ , respectively. In this analysis, single spectrum  
 254 fits were obtained at a given pressure by using the calculated Doppler width, setting the line shift  
 255 parameters  $\Delta_0 = \Delta_2 = 0$ , and by floating the five parameters  $A, \nu_0, \Gamma_0, \Gamma_2$ , and  $\nu_{vc}$ . We also  
 256 investigated the extent to which the fitted area depended on either of two physical constraints for

257 the parameters  $\Gamma_2/\Gamma_0$  and  $\nu_{vc}$ . The two constraints are:  $\Gamma_2/\Gamma_0 = (1-n) \frac{2}{3} \frac{m_p/m_a}{1+m_p/m_a}$  [18] and

258  $\nu_{vc} = k_B T / (2\pi m_a D)$  where  $n$  is the temperature exponent for the broadening coefficient,  $m_p/m_a$   
 259 is the perturber-to-absorber mass ratio,  $k_B$  is the Boltzmann constant, and  $D$  is the mass diffusion  
 260 coefficient of the CO<sub>2</sub> in N<sub>2</sub> (assumed to be proportional to pressure and equal to 0.16 cm<sup>2</sup> s<sup>-1</sup> at  $p$   
 261 = 101 kPa) [19]. We found essentially identical fitted areas (to within the fit uncertainties at the  
 262 0.05 % level) for all cases considered.

263 In addition to capturing more of the collisional physics as compared to the standard Voigt  
264 profile, our analysis is consistent with previous studies in which the qSDNGP yielded relatively  
265 small systematic fit residuals while introducing minimal uncertainty in the measured line areas [9].  
266 The highest fit quality QF (defined below) was obtained for the R16 line at transition wave number  
267  $\tilde{\nu}_0 = 4\,989.971\,515\text{ cm}^{-1}$  (QF = 4 200) at a pressure of  $p = 26.8\text{ kPa}$  using mixture A. This spectrum  
268 resulted in an individual relative fit uncertainty for the line area  $A$  equal to 0.01 %. As expected,  
269 the fitted area obtained after setting  $\Gamma_2 = \nu_{vc} = 0$  (which corresponds to the Voigt profile case)  
270 gave peak areas that were systematically low of those obtained using the qSDNGP by more than  
271 0.5%.

272  $\text{CO}_2$  and background  $\text{H}_2\text{O}$  interferences were assigned based on tabulated positions given  
273 in HITRAN 2012, and their respective Voigt profiles were used by fixing the Doppler width to its  
274 calculated value and floating the peak area and Lorentzian width. Also, lines R16 through R28  
275 were fitted using the constrained far-wing contributions of the neighboring target lines using the  
276 qSDNGP. However, we identified three cases of interferences which required more detailed  
277 analysis to optimize fit residuals, including: 1) weak  $^{12}\text{C}^{16}\text{O}_2$  lines partially overlapping with the  
278 strong target lines and detuned by 2 GHz to 3 GHz (R16, R20 and R24), 2) overlapping  $^{13}\text{C}^{16}\text{O}_2$   
279 lines within 1 GHz of the target lines (R22, R32, R46 and R53), and 3) partially overlapping water  
280 vapor lines (intensities ranging from  $10^{-25}\text{ cm/molec.}$  to  $10^{-23}\text{ cm/molec.}$  (R18, R24 and R42). In  
281 cases 1 and 3, the total area of the interferences plus the target lines was fit simultaneously to  
282 optimize the fit residuals. Subsequently, the model for total area was refit to the data by  
283 constraining the line intensity ratio ( $S_{\text{interference}}/S_{\text{target}}$ ) using either HITRAN 2012 [14] values or  
284 those in the UCL database [20]. This two-step fitting procedure was necessary to ensure that the  
285 fitting algorithm converged to a result exhibiting minimal residual peak area, consistent with  
286 literature values for the interfering intensities. The choice of the database affected the resulting  
287 target intensity  $S_{\text{target}}$  by less than 0.01 %. The same procedure was followed for case 2, although  
288 the first step (fitting the total area and then constraining) was omitted. The difference between  
289 constrained and unconstrained fits was biggest for case 2 ( $^{13}\text{CO}_2$  interferences) and was  
290 approximately 0.5 % for the R46 and R52 lines.

291 We note that the level of background water vapor varied strongly with time in our  
292 experiment. Based on fitted areas and published water vapor line intensities, the molar fraction of  
293 water vapor in our samples decreased tenfold over a time of one week from nearly 300  $\mu\text{mol/mol}$

294 down to about 30  $\mu\text{mol/mol}$ . We attribute this decrease to water vapor desorbing from the  
 295 bounding surfaces of the ring-down cell after exposure to room air. Of the three target transitions  
 296 where water vapor absorption was modeled, only the R42e line was significantly influenced by an  
 297 overlapping water line. Representative spectra for this transition are given in Fig. 3. Moreover,  
 298 this specific interference was problematic only for water vapor molar fractions greater than about  
 299 100  $\mu\text{mol/mol}$ . In this case, only spectra acquired with water vapor concentrations below this level  
 300 were considered in the final analysis.

301

### 302 3.2 *Rescaling to account for temperature variations*

303 Drift in the laboratory conditions during spectral acquisition led to changes in the  
 304 temperature of the sample gas within the ring-down cell. During acquisition of individual spectra,  
 305 these data exhibited an average standard deviation of 0.038 K and a maximum excursion of 0.15  
 306 K. In the absence of any temperature correction, this variability may compromise the measurement  
 307 accuracy, especially for the high- $J$  transitions which have a relatively strong temperature  
 308 dependence to the line intensity (e.g. 1.34 %  $\text{K}^{-1}$  for  $J'' = 52$ ). In order to correct for this measured  
 309 effect, we rescaled the spectra at each frequency step by accounting for the temperature  
 310 dependence of the total gas number density, line intensity, and the Lorentzian half-width. Unlike  
 311 the temperature, the measured total gas pressure was observed to be constant within a range of  
 312  $\pm 0.02$  % of the mean value, and hence this quantity was treated as a constant during each spectrum  
 313 acquisition.

314 Here we assume ideal gas law conditions (maximum relative uncertainty of 0.006 % at the  
 315 sample conditions), where the sample number density at each frequency step is

$$316 \quad n_q = \chi_{\text{CO}_2} \frac{p}{k_B T_q} \quad (3)$$

317 in which the index  $q$  indicates the frequency step,  $\chi_{\text{CO}_2}$  is the molar fraction of  $\text{CO}_2$ , and  $p$  and  $T_q$   
 318 are the measured pressure and temperature of the gas sample at each frequency step, respectively.

319 Considering only the target line of intensity  $S(T_q)$ , the uncorrected, measured absorption  
 320 coefficient associated with this transition is

$$321 \quad \alpha_q(\Delta\nu_q) = n_q c S(T_q) g(\delta\nu_q, \Gamma_0(T_q)) \quad (4)$$

322 where we have dropped the transition index  $n$  used in Eq. 2 and where  $\delta\nu_q$  is the spectrum  
 323 detuning relative to line center.

324 We assume that the rescaling of the data affects only the absorptive part of the measured  
 325 spectrum, without altering the base losses of the ring-down cavity. It follows that it is sufficient to  
 326 define an excess absorption  $\Delta\alpha_q = \alpha_q(T_q) - \alpha_q(\bar{T})$  of the target transition relative to its expected  
 327 value at the mean spectrum temperature  $\bar{T}$ . At each frequency step  $q$  we can write,

$$328 \quad \Delta\alpha_q = \alpha_{fit,q}(f_{norm,q} - 1), \quad (5)$$

329 with the normalization factor as the product of three temperature-dependent ratios,

$$330 \quad f_{norm,q} = \frac{T_q}{\bar{T}} \frac{S(\bar{T})}{S(T_q)} \frac{g(\delta\nu_q, \Gamma_0(\bar{T}))}{g(\delta\nu_q, \Gamma_0(T_q))}. \quad (6)$$

331 Here  $\alpha_{fit,q}$  is the absorption coefficient obtained by fitting the assumed line profile (qSDNGP) and  
 332 a linear baseline to the uncorrected data assuming a constant temperature of  $\bar{T}$ .

333 The line intensity ratio in Eq. 6 depends upon the molecular partition function  $Q(T)$  as  
 334 well as the energy of the lower-state rovibrational level  $E''$  [21]. We used the partition function  
 335 for  $^{12}\text{C}^{16}\text{O}_2$  which is calculated from direct summation and based on the variational calculations of  
 336  $E''$  given by Huang et al. [22]. This new partition function has been adopted by HITRAN 2016  
 337 [23] and differs by approximately  $-0.3\%$  from the previous calculation used in HITRAN 2012 at  
 338 the standard reference temperature  $T_r = 296$  K. We note however, that the old and new calculations  
 339 for the ratio  $Q(T)/Q(T_r)$  differ by less than  $0.003\%$  over the temperature range of 290 K to 300 K.  
 340 In terms of the partition function and associated parameters, the scaling factor used in converting  
 341 the line intensity from  $T$  to  $\bar{T}$  was modeled as

$$342 \quad \frac{S(\bar{T})}{S(T)} = \frac{Q(T_q)}{Q(\bar{T})} \exp\left[-\frac{hcE''}{k_B} \left(\frac{1}{\bar{T}} - \frac{1}{T_q}\right)\right]. \quad (7)$$

344 The line profile ratio in Eq. 7 was evaluated assuming a standard power-law dependence  
 345 for  $\Gamma_0(T_q) = \Gamma_0(\bar{T}) \left(\frac{\bar{T}}{T_q}\right)^n$  where  $n$  is again the temperature exponent for the broadening coefficient  
 346 (ranging from 0.69 to 0.76 for the measured lines) as specified in HITRAN 2012 for the case of  
 347 air-broadening. For the purposes of this correction, all other qSDNGP line profile parameters  
 348 (except for  $\Gamma_D$ ) were assumed to be independent of temperature.

349 With the preceding definitions, the corrected total loss-per-unit length measured at each  
 350 step  $q$  was evaluated as

351 
$$\frac{1}{c\bar{\tau}_{corr}(\Delta\nu_q)} = \frac{1}{c\bar{\tau}(\Delta\nu_q)} + \Delta\alpha_q = \frac{1}{c\bar{\tau}(\Delta\nu_q)} + \alpha_{fit,q}(f_{norm,q} - 1). \quad (8)$$

352 We subsequently fit Eq. 8 to the corrected total losses by floating the five parameters  $A, \nu_0, \Gamma_0, \Gamma_2$   
 353 and  $\nu_{vc}$ , thereby providing a peak area  $A(\bar{T})$  that corresponds to the spectrum-averaged  
 354 temperature  $\bar{T}$ . Given the small correction, only one iteration of the algorithm was implemented  
 355 in rescaling the spectrum.

356

### 357 3.3 Standard Line Intensity Determination

358 In order to determine the line intensity at  $T_r = 296$  K we also normalized each measured  
 359 peak area  $A(\bar{T}) \equiv A_{296}$  using

360 
$$\frac{A_{296}}{A(\bar{T})} = \frac{\bar{T}}{T_r} \frac{S(T_r)}{S(\bar{T})} = \frac{\bar{T}}{T_r} \frac{Q(\bar{T})}{Q(T_r)} \exp\left[-\frac{hcE''}{k_B} \left(\frac{1}{T_r} - \frac{1}{\bar{T}}\right)\right]. \quad (9)$$

361 Using the relationship between peak area (in GHz/cm), absorber number density and intensity  
 362 gives the following linear correspondence between  $A_{296}$  and  $p$ ,

363 
$$A_{296} = S_{296} c n_{CO_2}(p, T_r), \quad (10)$$

364 in which  $S_{296}$  and  $n_{CO_2}(p, T_r)$  are the line intensity in units of  $\text{cm}^{-1}/(\text{cm}^{-2} \text{ molec.})$  and number  
 365 density of  $\text{CO}_2$ , respectively at  $T_r$ . The linear correspondence assumed in Eq. 10, where we have  
 366 integrated over the normalized line profile (i.e.,  $\int g(\nu) d\nu = 1$ ), was rigorously evaluated for all  
 367 transition intensities reported herein (see Section 5).

368 The reported line intensities and standard uncertainties were obtained by weighted linear  
 369 regression (with 0-intercept) of the  $A_{296}$  vs.  $n_{CO_2}(p, T_r)$  data using Eq. 10, thus yielding a slope  
 370 equal to  $S_{296}c$ . In each linear regression, the weighting factors were given by  $1/\sigma_A^2$  where  $\sigma_A(p)$   
 371 is the standard error in the fitted peak area at pressure  $p$ . This uncertainty scales inversely with the  
 372 observed quality-of-fit (QF) factor for the chosen line profile [24]. We note that this type of  
 373 regression analysis is equivalent to a weighted average of the  $S_{296}$  values obtained from Eq. 10  
 374 where the respective weighting factors are given by  $1/(p\sigma_A^2(p))$ . Figure 3 illustrates the linear  
 375 regression analysis for the R36 transition. Because the derived line intensity depended upon  
 376 multiple spectra which were measured over time intervals typically exceeding one week, the slope

377 uncertainties determined above account for the majority of the Type A (statistical) uncertainty in  
378  $S_{296}$ . As discussed below, this component of the overall uncertainty can be assigned to statistical  
379 variability in sample conditions and noise in the measured ring-down spectra.

380

381

#### 382 **4 Evaluations of Measurement Uncertainty**

383 Combined uncertainties in  $S_{296}$  reported herein include both the type A (statistical) and type  
384 B (systematic) experimental uncertainties. Apart from the transition-dependent uncertainty in the  
385 temperature renormalization and the slightly different uncertainties on the sample gases (0.04 %  
386 and 0.06 % for mixtures A and B, respectively), the Type B relative uncertainties in  $S_{296}$  (for  
387 mixture B) are nearly the same for all measured transitions and range from 0.072 % to 0.092 %.  
388 An example calculation of combined Type B uncertainty for the R36 transition is shown in Table  
389 1. The component relative standard uncertainties assigned to temperature, pressure, non-ideal gas  
390 effects, isotopologue relative abundance, spectrum detuning axis (FSR), choice of line profile, and  
391 CO<sub>2</sub> molar fraction are (0.003 %, 0.009 %, 0.006 %, 0.01 %, 0.03 %, 0.05 %, 0.06%), respectively,  
392 resulting in a relative combined standard Type B uncertainty of 0.084 %.

393 The most important contributors to the Type B uncertainty are the choice of line profile,  
394 FSR determination, and CO<sub>2</sub> molar fraction. Of these three quantities, the FSR could be reduced  
395 below 0.000 5 % (1 kHz) relative uncertainty with higher-precision methods that use a more stable  
396 cavity locking reference laser and/or optical frequency comb as described in Ref. [10]. However,  
397 substantial reduction in the uncertainty of the line profile awaits advanced theoretical treatments  
398 that will require experimental validation. Likewise, substantial reduction in the uncertainty of the  
399 sample gas CO<sub>2</sub> molar requires challenging technical advances in gravimetric preparation and  
400 mitigation of surface adsorption/desorption effects that alter the relative abundance of CO<sub>2</sub> within  
401 the sample chamber over time.

402 Also shown in Table 1 is the Type A uncertainty for the R36 transition. This value was  
403 estimated to be 0.075 % based on the slope uncertainty of the weighted linear regression for the  
404  $A_{296}$  vs.  $p$  data. We note that these measurements spanned roughly one week and were subject to  
405 relatively long-term variations in the spectrometer performance. As expected, the measured Type  
406 A relative uncertainties tended to decrease as the line intensity and spectrum QF increased.

407 However, variations in the sample conditions achieved over long time scales likely dominated the  
408 Type A uncertainty for all cases considered. We found that measurements of  $S_{296}$  which were  
409 repeated several months apart exhibited similar variation (0.15 %) as that resulting from a set of  
410  $A_{296}$  vs.  $p$  data which was acquired over a much shorter (week-long) time scale.

411 The most likely source of irreproducibility in the measured intensity would be caused by  
412 temperature- and flow-dependent interactions of the  $\text{CO}_2$  with the internal surfaces of the ring-  
413 down cell. Although the measurements were always done under flowing conditions to mitigate  
414 wall effects, the duty cycle of spectrum acquisition was well below 100 %. During the dormant  
415 times, we kept a static charge within the ring-down cell to conserve sample gas. Under these  
416 conditions,  $\text{CO}_2$  tends to adsorb to the walls of the ring-down cell, and thereafter desorb as gas  
417 flow resumed prior to spectrum acquisition. In order to investigate this effect, we measured  
418 intensities of a several transitions at two flow rates and for two  $\text{CO}_2$  molar fractions, by quantities  
419 varying by a factor of two. For all cases, measurement reproducibility was better than 0.15 %, and  
420 comparable to the long-term Type A measurement uncertainty.

421 Intensities for seven of the  $\text{CO}_2$  transitions investigated here were measured using both  
422 photoreceivers described in Sec. 2.8. Relative differences between the measured intensities  
423 encompassing these transitions had a standard deviation of 0.43 % which was dominated by the  
424 higher noise level of the InGaAs photoreceiver. Also, because the average relative difference in  
425 line intensity was 0.35 % and comparable to the standard deviation, this comparison provided no  
426 evidence of systemic effects on measured line intensity associated with our choice of  
427 photoreceiver.

428

429

## 430 **5 Results**

431 As an illustrative example, we present the measurement of the R36 line intensity at  $\tilde{\nu}_0 =$   
432  $5\,001.49871\text{ cm}^{-1}$ . Three representative spectra spanning 14 GHz of tuning range are plotted in the  
433 top panel of Fig. 4. Results are shown for mixture A at three constant pressure conditions:  
434 6.78 kPa, 20.16 kPa, and 33.54 kPa, respectively. The measured spectra (colored markers)  
435 comprised a single  $\text{CO}_2$  transition, centered at a frequency detuning of  $\delta\nu_0 = 0$ . The spectra were  
436 fit (solid lines) using the qSDNGP, and the fit residuals with a standard deviation of  $8 \times 10^{-10}\text{ cm}^{-1}$

437 are plotted in the bottom panel (solid lines with markers). For the R36 transition, the highest  
438 observed quality-of-fit factor was  $QF = 1\,700$  at  $p = 20.16$  kPa.

439 Temperature-corrected fitted line areas for several transitions are plotted vs. number  
440 density in Fig. 5, along with the corresponding fit uncertainties and fit residuals. Continuing with  
441 the illustrative example, an unweighted linear regression of  $A_{296}$  vs. number density for the R36  
442 line yielded  $S_{296} = 3.904 \times 10^{-22}$  cm/molec. with a combined standard uncertainty of  $u_r(S_{296}) = 7$   
443  $\times 10^{-25}$  cm/molec. (see Table 1, relative combined standard uncertainty of 0.18 %). The fit  
444 residuals plotted in the bottom panel, with a standard deviation of  $0.005$  kHz cm<sup>-1</sup>, illustrate the  
445 observed high degree of linearity in the measured values of  $A_{296}$  vs. number density.

446 A list of measured intensities for 19 transitions of the (20012) - (00001) <sup>12</sup>C<sup>16</sup>O<sub>2</sub> band  
447 ranging from R16 to R52 can be found in Table 2. These data span the wave number range  $4\,989$   
448 cm<sup>-1</sup> to  $5\,009$  cm<sup>-1</sup>. Included for comparison are intensities from both HITRAN 2012 [14, 25] and  
449 the Carbon Dioxide Spectroscopic Databank (CDS-296) [26]. We also compare the NIST data  
450 to rovibrational line intensities calculated by Zak et al. (UCL) using various semi-empirical and  
451 *ab initio* potential energy surfaces (PES) in combination with an *ab initio* dipole moment surface  
452 (DMS) for <sup>12</sup>C<sup>16</sup>O<sub>2</sub> [20] as well as those calculated by Huang et al. (Ames-2016) using a semi-  
453 empirically refined PES and an *ab initio* DMS [27].

454

455

## 456 **6 Discussion**

### 457 *6.1 Comparison with the literature – databases*

458 For comparison between existing databases and our highly accurate intensities we define  
459 the relative difference  $\varepsilon = S_i/S_{NIST} - 1$ , where  $S_i$  are either the HITRAN 2012 [14, 25], CDS-  
460 296 [26], Ames-2016 [27], or UCL [20, 23] intensities and  $S_{NIST}$  the corresponding measured NIST  
461 intensities. Values of  $\varepsilon$  are given in Table 2, and plotted in Fig. 6. The tabulated HITRAN 2012  
462 line intensities, which originated from Ref. [25], differ from those reported here by as much as  
463  $-3$  %. The magnitude of this difference is larger for more intense lines, and changes sign at higher  
464 rotational quantum numbers ( $m = J'' + 1$  for R-branch transitions). A systematic deviation of this  
465 magnitude is significantly larger than the target uncertainties of current and future remote sensing  
466 campaigns [1-4].

467 Smaller systematic deviations with magnitude of approximately 1 % are also observed for  
468 CDS-296 ( $\bar{\varepsilon} = -1.1 \%$ ), where  $\bar{\varepsilon}$  is the mean value of all  $\varepsilon$  plotted in Fig. 6. Of the line list  
469 databases considered here, the recently reported *ab initio* intensities from UCL [20] and Ames-  
470 2016 [27] exhibit the best agreement with our measurements, with average relative differences of  
471  $\bar{\varepsilon} = -0.20 \% \pm 0.27 \%$  and  $\bar{\varepsilon} = -0.26 \% \pm 0.27 \%$ , respectively. This level of agreement between  
472 theoretical *ab initio* and experimental line intensities is similar to that demonstrated in a recent  
473 study of the (30013) - (00001)  $^{12}\text{C}^{16}\text{O}_2$  band, where the UCL *ab initio* calculations and NIST FS-  
474 CRDS measurements yielded  $\bar{\varepsilon} = -0.33 \%$  and  $\sigma_{\varepsilon} = 0.23 \%$  [28].

475 The high-level agreement between rigorous experimental measurements of  $^{12}\text{C}^{16}\text{O}_2$   
476 transitions intensities and those calculated by UCL using *ab initio* quantum chemistry methods  
477 has, in large part, motivated the further integration of the UCL database into the most recent edition  
478 of HITRAN 2016 (see Section 2.2, including Fig. 7, of Ref [23]). The continued benchmarking of  
479 *ab initio* intensities against experimental measurements of the highly abundant isotopologues (i.e.,  
480  $^{12}\text{C}^{16}\text{O}_2$ ) enables the confident inclusion of calculated line list parameters for hot-band lines, rare  
481 and clumped isotopologues and other low-abundance species that are difficult to measure  
482 experimentally with sufficient accuracy and precision.

483

## 484 6.2 Comparison with literature – individual experiments

485 In Fig. 7, intensity measurements reported by the French National Center for Scientific  
486 Research (CNRS, blue circles) [29] and the Seconda Università di Napoli (SUN, red diamonds  
487 and magenta inverted triangles) [30-32] are shown to be in modest agreement with the NIST  
488 values. However, the claimed uncertainty in the SUN intensities appears largely underestimated  
489 [30- 32], especially for the R16e and R18e transitions [31, 32]. The underestimated uncertainties  
490 in the SUN data were eluded to by Wübbeler et al. in a detailed study of the R12 transition intensity  
491 [33]. Recent work by Odintsova et al. [34] revisited the R2, R4, and R6 rovibrational transitions  
492 using optical feedback cavity enhanced absorption spectroscopy (OF-CEAS) referenced to an  
493 optical frequency comb, multispectral fitting, and the HTP, and subsequently identified the source  
494 of the underestimated intensities and uncertainties as 1) the choice of line profile (GP and NGP  
495 [32] vs. HTP [34]) and 2) the use of low-accuracy pressure gauges in Ref. [31-32]. As state in  
496 Section 3.1, we note that the use of specific limiting cases of the HTP (such as the Voigt profile)

497 to fit spectra reported herein resulted in the systematic underestimation of the transition intensity  
498 on the order of 0.5 %.

499 Figure 7 also serves to illustrate the comprehensive nature (19 individual transitions  
500 measured with absolute accuracy between 0.15 % and 0.46 %) of this NIST experimental study of  
501 transitions intensities throughout the R-branch of the (20012) - (00001)  $^{12}\text{C}^{16}\text{O}_2$  band near  $\lambda = 2$   
502  $\mu\text{m}$ .

503

### 504 6.3 Detailed comparison with the UCL *ab initio* DMS (HITRAN 2016)

505 Returning to the comparison with the UCL database, several experimental measurements  
506 of the (20012) - (00001)  $^{12}\text{C}^{16}\text{O}_2$  band, as well as the CDS-296 values, are again plotted vs.  $m$  in  
507 Fig. 8, but this time, relative to the UCL *ab initio* intensities. In Fig. 8, we define  $\varepsilon_{UCL} = S_i/S_{UCL} -$   
508 1, where  $S_{UCL}$  are the intensities calculated by Zak et al. [20] and recently adopted by HITRAN  
509 2016 [23], and  $S_i$  are values from NIST (reported herein), University of Naples II (UniNA2) [34],  
510 Physikalisch-Technische Bundesanstalt (PTB) [33], and CDS-296 [26], respectively. In the top  
511 panel, the range of lower-state rotational quantum numbers is expanded to include both P- and R-  
512 branch transitions of  $|m| \leq 60$ , currently outside of the tuning range of the NIST instrument. This  
513 overview of the (20012) - (00001)  $^{12}\text{C}^{16}\text{O}_2$  band reveals a subtle yet significant trend in  $\varepsilon_{UCL}$  vs.  
514  $|m|$  for both the combined NIST + PTB + UniNA2 high-precision data set and CDS-296.

515 Also plotted relative to the UCL data base [20, 23] in the top panel of Fig. 8 are the Ames-  
516 2016 intensities [27]. An unphysical discontinuity appears in Ames-2016 as  $|m| \rightarrow 0$ , attributed  
517 to a known basis set convergence error [27]. An update to Ames-2016 which eliminates this so-  
518 called “ $J$ -jump” is promised [27]. Given the estimates in Section 3.1 of [27], the Ames-2016 update  
519 will most likely decrease slightly the level of agreement between NIST and Ames-2016 quantified  
520 in Section 6.1 of this manuscript by approximately 0.25 % to 0.3 %, or approximately half of the  
521 reported usual “ $J$ -jump” splitting of 0.5 % to 0.6 % observed in Ames-2016 for the symmetric  $\text{CO}_2$   
522 isotopologues.

523 A detailed look at the highly accurate R-branch data is shown in the bottom panel of Fig.  
524 8. Superimposed upon the combined data set of NIST + PTB + UniNA2 is a quadratic regression  
525 (dotted black line) of the CDS-296 intensities, shifted by  $\delta_{\varepsilon_{UCL}} = +1.1$  % relative to the CDS-  
526 296 values (open circles). The shift value  $\delta_{\varepsilon_{UCL}}$  was estimated from the average relative deviation  
527  $S_i/S_{CDS-296} - 1$ , where  $S_i$  are the individual transition intensities within the combined NIST + PTB

528 + UniNA2 data set (19 NIST transitions, 1 PTB transition, and 3 UniNA2 transitions, respectively)  
529 and  $S_{CDSD}$  are the corresponding CDSD-296 intensities.

530 Rationale for the magnitude and sign of the empirical shift parameter  $\delta_{\epsilon_{UCL}}$  is found by  
531 studying the origins of the (20012) - (00001)  $^{12}\text{C}^{16}\text{O}_2$  band intensities predicted by CDSD-296  
532 [26]. In Section 4.2 of Ref. [26], Tashkun et al. reported a direct comparison between CDSD-296  
533 predictions and the 9 transition intensities of Casa et al. [32], noting good agreement (within  
534 reported experimental error). It is now accepted, however, from Refs. [33-34] and from this work,  
535 that the intensity measurements of Casa et al. [31-32] were systematically low due to the choice  
536 of line profile, and that the quoted accuracy was overestimated [34]. For the R2, R4, R6, R12, R16,  
537 and R18 transitions, we find that  $S_i$  from the combined NIST + PTB + UniNA2 data set are, on  
538 average, 1.6 % greater than  $S_i$  reported by Casa et al. [32]. We therefore postulate that the Casa et  
539 al. measurements influenced the systematic shift in the CDSD-296 intensities predicted for the  
540 (20012) - (00001)  $^{12}\text{C}^{16}\text{O}_2$  band, as evidenced by the empirical shifting factor  $\delta_{\epsilon_{UCL}} = 1.1$  %.

541 Beyond the systematic shift parameter  $\delta_{\epsilon_{UCL}}$  (which is independent of  $m$ ), a subtle yet  
542 significant trend in  $\epsilon_{UCL}$  vs.  $m$  was observed for the combined NIST + PTB + UniNA2 intensities.  
543 Inspection of the black dotted line in the bottom panel of Fig. 8 reveals that the magnitude and  
544 sign of the trend in  $\epsilon_{UCL}$  vs.  $m$  observed for the combined NIST + PTB + UniNA2 experimental  
545 intensities agree with the quadratic trend predicted by CDSD-296 using an effective Hamiltonian  
546 and DMS. This trend in experimental and semi-empirical data sets, whether quadratic or otherwise,  
547 could indicate the limited accuracy with which quantum chemistry calculations of  $S$  performed  
548 using a full *ab initio* DMS [20] predict the  $m$ -dependence of the line intensity. Similar trends have  
549 also recently been observed in the high-resolution Fourier transform spectroscopy of the (20013)  
550 - (00001) and (30013) - (00001)  $^{12}\text{C}^{16}\text{O}_2$  bands [35, 36]. Semi-classical spectroscopic expressions  
551 for  $S_v$  (the total vibrational band intensity) generalized using perturbation theory to include  
552 vibration-rotation interactions via the  $F$ -factor often are used to fit residual  $m$ -dependence in the  
553 line intensity that is not captured by the standard Hönl-London factors. For the so-called parallel  
554 bands of  $\text{CO}_2$  where  $\Delta l = 0$ , this factor is modeled as  $F = (1 + a_1 m + a_2 m^2 + a_3 m^3)^2$  [36-39],  
555 where  $F$ , and  $a_x$  are the Herman-Wallis coefficients which model perturbations to the standard  
556 rigid-rotor Hamiltonian (i.e., vibration-rotation interactions) [40]. Without corresponding accurate  
557 FS-CRDS measurements of numerous transitions intensities within the P-branch ( $m < 0$ ) of the

558 (20012) - (00001)  $^{12}\text{C}^{16}\text{O}_2$  band, however, it is premature to fit the  $F$ -factor and definitively report  
559 updated, values of  $S_v$  and  $a_x$  [39]. This is the focus of ongoing and future experiments at NIST.

560

561

## 562 **7 Conclusion**

563 We report experimentally determined line intensities throughout the R-branch of the  
564 (20012) - (00001) band of  $^{12}\text{C}^{16}\text{O}_2$  near  $\lambda = 2 \mu\text{m}$ . These intensities, measured by frequency-  
565 stabilized cavity ring-down spectroscopy, provide the most stringent experimental test of *ab initio*  
566 dipole moment and potential energy surfaces. Benchmarking *ab initio* calculations at standard  
567 conditions is a prerequisite for establishing the validity of extrapolating calculated molecular  
568 reference data to extreme thermodynamic and exotic kinetic conditions [41]. As was the case for  
569  $^{12}\text{C}^{16}\text{O}_2$  intensities at  $\lambda \approx 1.6 \mu\text{m}$  [28], *ab initio* calculations of the line intensities are overall found  
570 to be in excellent agreement with our high-accuracy experimental values. The further validation  
571 of theory (both *ab initio* and semi-empirical effective Hamiltonian approaches) by high-accuracy  
572 measurements of experimental reference data will undoubtedly expand our understanding of  
573 planetary and atmospheric sciences by enabling increasingly precise remote sensing missions.

574

575

576 **ACKNOWLEDGEMENTS:** The authors acknowledge funding from the National Institute of  
577 Standards and Technology (NIST) Greenhouse Gas Measurements Program. We thank George C.  
578 Rhoderick, Michael E. Kelly, Kimberly Harris of the NIST Gas Sensing Metrology Group for  
579 gravimetrically preparing and certifying gas cylinders of precisely known  $\text{CO}_2$  molar fractions.  
580 We also acknowledge the experimental assistance and expertise of Mélanie Ghysels (NIST), and  
581 thank Eleanor Waxman (NIST) for comments on the manuscript.

582

583

584 **REFERENCES:**

585

- 586 1. F. Oyafuso, V. H. Payne, B. J. Drouin, V. M. Devi, D. C. Benner, K. Sung, S. Yu, I. E.  
587 Gordon, R. Kochanov, Y. Tan, et al., *J. Quant. Spectrosc. Radiat. Transfer* **203**, 213-223  
588 (2017).
- 589 2. D. R. Thompson, D. C. Benner, L. R. Brown, D. Crisp, V. M. Devi, Y. Jiang, V. Natraj, F.  
590 Oyafuso, K. Sung, D. Wunch, et al., *J. Quant. Spectrosc. Radiat. Transfer* **113**, 2265-2276  
591 (2012).
- 592 3. D. Crisp, R. M. Atlas, F.-M. Breon, L. R. Brown, J. P. Burrows, P. Ciais, B. J. Conner, S. C.  
593 Doney, I. Y. Fung, D. J. Jacob, et al., *Adv. Space Res.* **34**, 700-709 (2004).
- 594 4. C. E. Miller, L. R. Brown, R. A. Toth, D. C. Benner, V. M. Devi, *C. R. Phys.* **6**, 876-887  
595 (2005).
- 596 5. J. T. Hodges, H. P. Layer, W. W. Miller, G. E. Scace, *Rev. Sci. Instrum.* **75**, 849-863 (2004).
- 597 6. D. A. Long, A. Cygan, R. D. van Zee, M. Okumura, C. E. Miller, D. Lisak, J. T. Hodges,  
598 *Chem. Phys. Lett.* **536**, 1-8 (2012).
- 599 7. J. T. Hodges, J. P. Looney, R. D. van Zee, *Appl. Opt.* **35**, 4112-4116 (1996).
- 600 8. J. T. Hodges and D. Lisak, *Appl. Phys. B* **85**, 375-382 (2006).
- 601 9. V. T. Sironneau and J. T. Hodges, *J. Quant. Spectrosc. Radiat. Transfer* **152**, 1-15 (2015).
- 602 10. H. Lin, Z. D. Reed, V. T. Sironneau, J. T. Hodges, *J. Quant. Spectrosc. Radiat. Transfer* **161**,  
603 11-20 (2015).
- 604 11. H. Huang and K. K. Lehman, *Appl. Opt.* **47**, 3817-3827 (2008).
- 605 12. A. J. Fleisher, D. A. Long, Q. Liu, J. T. Hodges, *Phys. Rev. A* **93**, 013833 (2016).
- 606 13. J. T. Hodges and R. Ciuryło, *Rev. Sci. Instrum.* **76**, 023112 (2005).
- 607 14. L. S. Rothman, I. E. Gordon, Y. Babikov, A. Barbe, D. C. Benner, P. F. Bernath, M. Birk, L.  
608 Bizzocchi, V. Boudon, L. R. Brown, et al., *J. Quant. Spectrosc. Radiat. Transfer* **130**, 4-50  
609 (2013).
- 610 15. D. Halmer, G. von Basum, P. Hering, M. Mürtz, *Rev. Sci. Instrum.* **75**, 2187-2191 (2004).
- 611 16. R. Ciuryło, *Phys. Rev. A* **58**, 1029-1039 (1998).
- 612 17. J. Tennyson, P. F. Bernath, A. Campargue, A. G. Császár, L. Daumont, R. R. Gamache, J. T.  
613 Hodges, D. Lisak, O. V. Naumenko, L. S. Rothman, et al., *Pure Appl. Chem.* **86**, 1931-1943  
614 (2014).

- 615 18. M. Ghysels, Q. Liu, A. J. Fleisher, J. T. Hodges, *Appl. Phys. B* **123**, 124 (2017).
- 616 19. W. J. Massmana, *Atmospheric Environ.* **32**, 1111-1127 (1998).
- 617 20. E. Zak, J. Tennyson, O. L. Polyansky, L. Lodi, N. F. Zobov, S. A. Tashkun, V. I. Perevalov,  
618 *J. Quant. Spectrosc. Radiat. Transfer* **177**, 31-42 (2016).
- 619 21. M. Simeckova, D. Jacquemart, L. S. Rothman, R. R. Gamache, A. Goldman, *J. Quant.*  
620 *Spectrosc. Radiat. Transfer* **98**, 130-155 (2006).
- 621 22. X. Huang, R. R. Gamache, R. S. Freedman, D. W. Schwenke, T. J. Lee, *J. Quant. Spectrosc.*  
622 *Radiat. Transfer* **147**, 134-144 (2014).
- 623 23. I. E. Gordon, L. S. Rothman, C. Hill, R. V. Kochanov, Y. Tan, P. F. Bernath, M. Birk, V.  
624 Boudon, A. Campargue, K. V. Chance, et al., *J. Quant. Spectrosc. Radiat. Transfer* **203**, 3-69  
625 (2017).
- 626 24. A. Cygan, D. Lisak, S. Wójtewicz, J. Domysławska, J. T. Hodges, R. S. Trawiński, R.  
627 Ciuryło, *Phys. Rev. A* **85**, 022508 (2012).
- 628 25. R. A. Toth, L. R. Brown, C. E. Miller, V. M. Devi, D. C. Benner, *J. Quant. Spectrosc.*  
629 *Radiat. Transfer* **109**, 906-921 (2008).
- 630 26. S. A. Tashkun, V. I. Perevalov, R. R. Gamache, J. Lamouroux, *J. Quant. Spectrosc. Radiat.*  
631 *Transfer* **152**, 45-73 (2015).
- 632 27. X. Huang, D. W. Schwenke, R. S. Freedman, T. J. Lee, *J. Quant. Spectrosc. Radiat. Transfer*  
633 **203**, 224-241 (2017).
- 634 28. O. L. Polyansky, K. Bielska, M. Ghysels, L. Lodi, N. F. Zobov, J. T. Hodges, J. Tennyson,  
635 *Phys. Rev. Lett.* **114**, 243001 (2015).
- 636 29. L. Régalia-Jarlot, V. Zéninari, B. Parvitte, A. Grossel, X. Thomas, P. von der Heyden, G.  
637 Durry, *J. Quant. Spectrosc. Radiat. Transfer* **101**, 325-338 (2006).
- 638 30. A. Castrillo, G. Gagliardi, G. Casa, L. Gianfrani, *Phys. Rev. A* **67**, 062503 (2003).
- 639 31. G. Casa, D. A. Parretta, A. Castrillo, R. Wehr, L. Gianfrani, *J. Chem. Phys.* **127**, 084311  
640 (2007).
- 641 32. G. Casa, R. Wehr, A. Castrillo, E. Fasci, L. Gianfrani, *J. Chem. Phys.* **130**, 184306 (2009).
- 642 33. G. Wübbeler, G. J. Padilla Viquez, K. Jousten, O. Werhahn, C. Elster, *J. Chem. Phys.* **135**,  
643 204304 (2011).
- 644 34. T. A. Odintsova, E. Fasci, L. Moretti, E. J. Zak, O. L. Polyansky, J. Tennyson, L. Gianfrani,  
645 A. Castrillo, *J. Chem. Phys.* **146**, 244309 (2017).

- 646 35. D. C. Benner, V. M. Devi, K. Sung, L. R. Brown, C. E. Miller, V. H. Payne, B. J. Drouin, S.  
647 Yu, T. J. Crawford, A. W. Mantz, et al., *J. Mol. Spectrosc.* **326**, 21-47 (2016).
- 648 36. V. M. Devi, D. C. Benner, K. Sung, L. R. Brown, T. J. Crawford, C. E. Miller, B. J. Douin,  
649 V. H. Payne, S. Yu, M. A. H. Smith, et al., *J. Quant. Spectrosc. Radiat. Transfer* **177**, 117-  
650 144 (2016).
- 651 37. R. A. Toth, *Appl. Opt.* **23**, 1825-1834 (1984).
- 652 38. V. M. Devi, D. C. Benner, M. A. H. Smith, L. R. Brown, M. Dulick, *J. Quant. Spectrosc.*  
653 *Radiat. Transfer* **76**, 393-410 (2003).
- 654 39. R. A. Toth, L. R. Brown, C. E. Miller, V. M. Devi, D. C. Benner, *J. Mol. Spectrosc.* **239**,  
655 221-242 (2006).
- 656 40. R. Herman and R. F. Wallis, *J. Chem. Phys.* **23**, 637-646 (1955).
- 657 41. J. Tennyson and S. N. Yurchenko, *Molecular Astrophysics* **8**, 1-18 (2017).
- 658

659 **Table 1.** Standard ( $1\sigma$ ) uncertainty components contributing to uncertainty in the  
660 measured intensity of the (20012) - (00001) band R36  $^{12}\text{C}^{16}\text{O}_2$  transition located at  
661  $\tilde{\nu}_0 = 5\,001.498\,71\text{ cm}^{-1}$ . The random (type A) relative standard uncertainty is  
662 dominated by the 0.15 % irreproducibility value in the intensities determined from  
663 repeating peak area vs. number density data sets. The systematic (type B)  
664 uncertainties are nearly identical for all transitions, the sole difference being caused  
665 by the transition-dependent sensitivity of the temperature correction.

Parameter	$u_r(S_{296})$ (%)	Description
<b>Type A</b>		
$A_{296}/n$	0.04	<sup>a</sup> from weighted regression of $A_{296}$ vs. $n$
$\langle A_{296}/n \rangle$	0.15	long-term measurement repeatability
<b>Type B</b>		
$(S(T_r)/S(T))(T/T_r)$	0.01	transition-dependent $T$ correction
$p$	0.01	pressure and non-ideal gas effects
$\chi_{CO_2}$	0.06	<sup>b</sup> sample molar fraction
$\chi_{626}$	0.01	isotopic abundance of $^{12}\text{C}^{16}\text{O}_2$
$\delta_{13C}$	0.04	$\delta_{13C}$ concentration
A (line shape)	0.05	<sup>c</sup> area uncertainty caused by choice of line profile
FSR	0.03	cavity free spectral range
<b>Combined Type B</b>	0.09	
<b>Combined Types A &amp; B</b>	0.18	

666 <sup>a</sup>Average value. Individual values for all lines range from 0.014 % to 0.14 %.

667 <sup>b</sup>Uncertainty ( $k = 1$ ) for gravimetrically prepared cylinder with  $\chi_{CO_2} = 49.826\ \mu\text{mol/mol}$   
668 (mixture A) the uncertainty is 0.04 %. For the cylinder with  $\chi_{CO_2} = 100.474\ \mu\text{mol/mol}$   
669 (mixture B), the uncertainty is 0.06 %.

670 <sup>c</sup>Based on variation of fitted peak area with chosen line profile.

671

672 **Table 2.** Intensities for the (20012) - (00001)  $^{12}\text{C}^{16}\text{O}_2$  band measured in this study, along with  
673 the corresponding total combined uncertainties. For comparison, we also list the relative  
674 differences  $\varepsilon = S/S_{\text{NIST}} - 1$  between literature values and the NIST intensities. All intensities  
675 are referenced to 296 K and to a relative abundance of 0.984 2 for the  $^{12}\text{C}^{16}\text{O}_2$  isotopologue.  
676

transition	$\tilde{\nu}_0^{\text{a}}$ ( $\text{cm}^{-1}$ )	$S_{296}$ ( $10^{-22}$ cm/molec.)	$u_r(S_{296})$ ( $10^{-24}$ cm/molec.)	UCL <sup>b</sup> $\varepsilon$ (%)	Ames <sup>c</sup> $\varepsilon$ (%)	CDS <sup>d</sup> $\varepsilon$ (%)	HITRAN 2012 <sup>a</sup> $\varepsilon$ (%)
R16e	4 989.971 52	13.27	2	-0.60	-0.69	-1.2	-3.0
R18e	4 991.258 51	12.98	2	-0.46	-0.52	-1.1	-2.8
R20e	4 992.515 74	12.37	2	-0.24	-0.31	-0.89	-2.5
R22e	4 993.743 17	11.542	1.9	-0.45	-0.49	-1.1	-2.5
R24e	4 994.940 78	10.529	1.8	-0.56	-0.64	-1.3	-2.6
R26e	4 996.108 54	9.387	1.6	-0.59	-0.65	-1.3	-2.6
R28e	4 997.246 41	8.178	1.4	-0.37	-0.42	-1.1	-2.2
R30e	4 998.354 39	6.961	1.2	0.19	0.13	-0.63	-1.6
R32e	4 999.432 44	5.853	1.0	0.034	-0.016	-0.82	-1.6
R34e	5 000.480 55	4.827	0.8	-0.062	-0.11	-0.97	-1.6
R36e	5 001.498 71	3.904	0.7	-0.051	-0.12	-1.0	-1.4
R38e	5 002.486 91	3.107	0.5	-0.23	-0.28	-1.2	-1.4
R40e	5 003.445 15	2.431	0.4	-0.49	-0.57	-1.5	-1.5
R42e	5 004.373 44	1.853	0.3	0.11	0.067	-1.0	-0.70
R44e	5 005.271 77	1.402	0.2	-0.29	-0.32	-1.4	-0.93
R46e	5 006.140 19	1.0350	0.19	0.097	0.037	-1.2	-0.29
R48e	5 006.978 70	0.7542	0.14	0.053	-0.027	-1.2	-0.15
R50e	5 007.787 36	0.5402	0.10	0.056	-0.031	-1.3	0.11
R52e	5 008.566 20	0.3804	0.08	0.079	-0.0018	-1.3	0.39

677 <sup>a</sup>[14, 25]

678 <sup>b</sup>[20, 23]

679 <sup>c</sup>Intensities at 296 K from Ames-2016 [27] were accessed online at <http://huang.seti.org> on  
680 25 September 2017.

681 <sup>d</sup>[26]

682

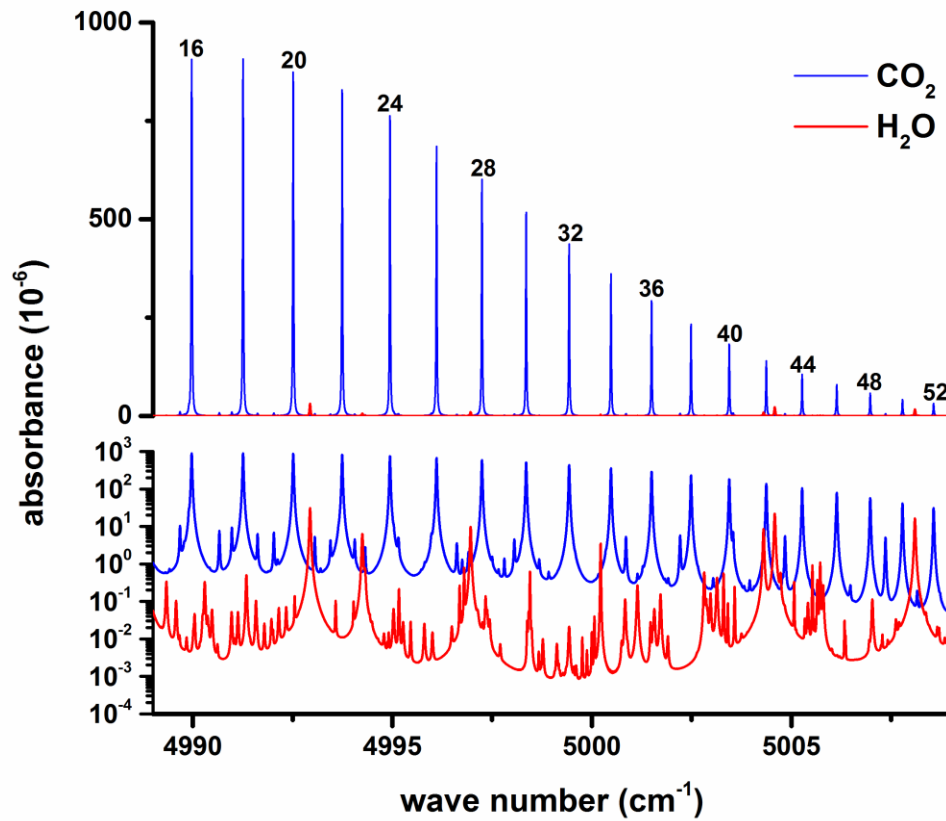


**Figure 1.** Simulated absorption spectrum for the spectral region of interest revealing the dominant  $^{12}\text{C}^{16}\text{O}_2$  band transitions and interferences from weaker carbon dioxide and water vapor transitions. Pressure and temperature of 133 kPa and 296 K, respectively, path length of 75 cm, and molar fractions of carbon dioxide and water vapor both equal to  $10^{-4}$ . Air-broadening is assumed and line parameters are based on HITRAN 2012. The lower-state angular momentum quantum number  $J'$  is indicated above every other (20012) - (00001)  $^{12}\text{C}^{16}\text{O}_2$  transition.

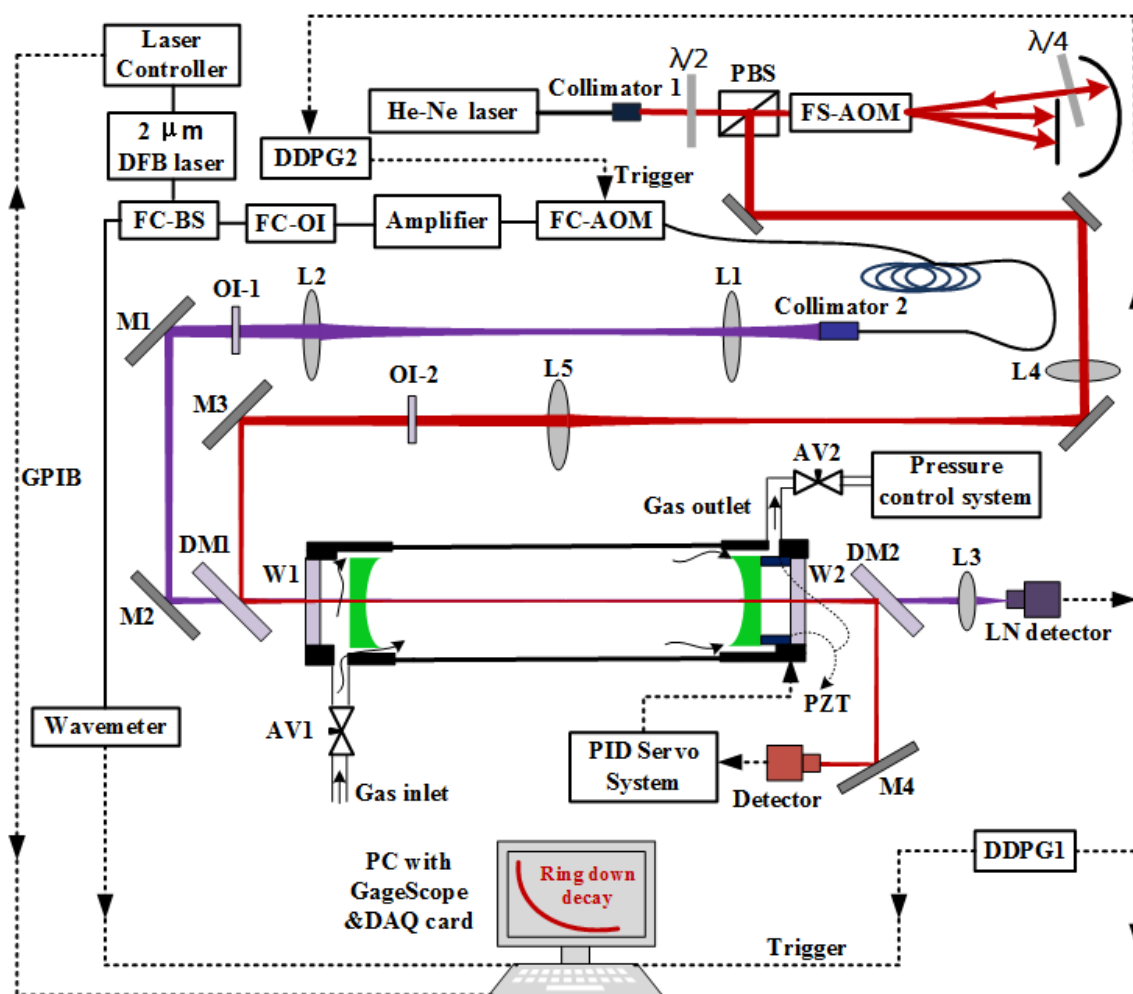


**Figure 2.** Schematic of the frequency-stabilized cavity ring-down spectroscopy (FS-CRDS) instrument. Free-space HeNe and DFB probe laser propagation is shown as solid red and blue lines/arrows, respectively. Electronics and radiofrequency cables are shown as solid black lines. Clockwise from the top left, acronyms and abbreviations used in the schematic are DFB, distributed feedback; FC, fiber-coupled; BS, beam splitter; OI, optical isolator, AOM, acousto-optic modulator, PBS, polarization beam splitter; L, lens; AV, valve; W, window; DM, dichoric mirror; LN, liquid nitrogen; PZT, piezo-electric transducer; PID proportional-integral-derivative; M, mirror; CCD, charge-coupled device; PC, personal computer; DDPG, digital delay pulse generator; DAQ, data acquisition; and ppm, parts-per-million.

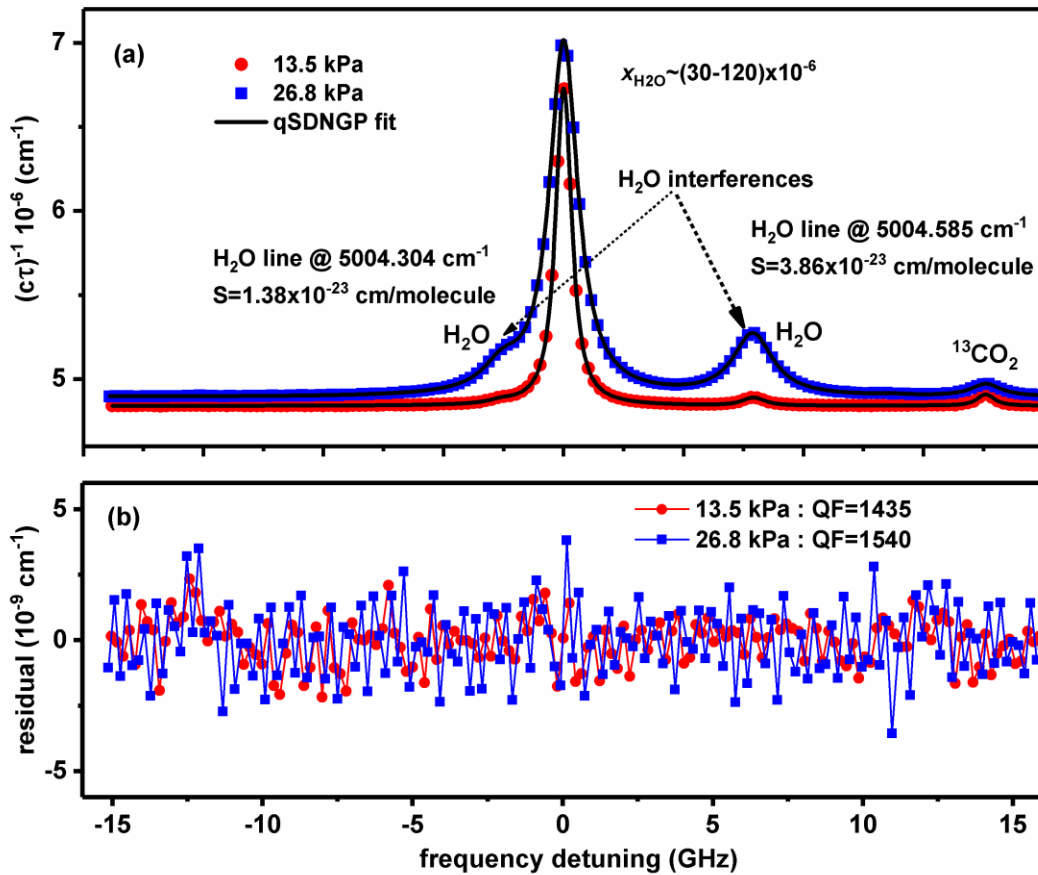


**Figure 3.** a) Spectrum of the (20012) - (00001) R42e  $^{12}\text{C}^{16}\text{O}_2$  transition in the presence of two different trace amounts of  $\text{H}_2\text{O}$ . Plotted in blue squares is the measured spectrum at a total pressure of  $P=26.830$  kPa and a fitted  $\text{H}_2\text{O}$  mole fraction of  $\chi_{\text{H}_2\text{O}} = 300$   $\mu\text{mol/mol}$ . For comparison, the same spectrum with a significantly smaller  $\chi_{\text{H}_2\text{O}}$  is plotted as red circles. Each spectrum was fitted to a sum of qSDNGPs (black lines), and broadening and transition frequency parameters for the  $\text{H}_2\text{O}$  interferences were held fixed to known values [14]. (b) Even in the presence of a large  $\chi_{\text{H}_2\text{O}}$ , the QF factor and noise on the residuals is for all intents and purposes identical for both spectra shown in (a).

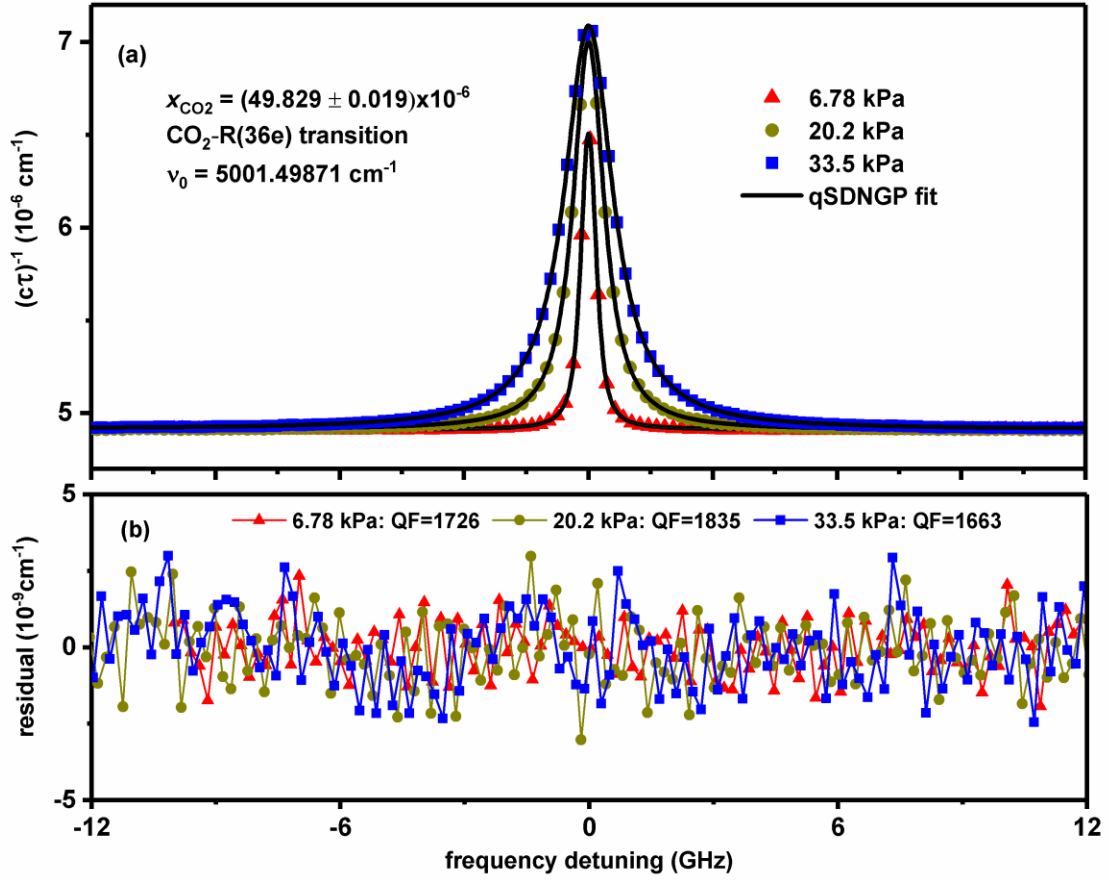


**Figure 4.** (a) Absorption spectrum of the R36e transition within the (20012) - (00001)  $^{12}\text{C}^{16}\text{O}_2$  band recorded at pressures of  $P = 6.78$  kPa (red triangles),  $p = 20.2$  kPa (green circles), and  $p = 33.5$  kPa (blue squares), respectively. Fitted models using the quadratic speed-dependent Nelkin-Ghatak profile (qSDNGP) are plotted as solid black lines. (b) Fit residuals (observed minus calculated) for the three spectra shown in (a). The quality-of-fit (QF) is defined as  $\text{QF} = (\alpha_{\max} - \alpha_{\min}) / \sigma_f$ , where  $\sigma_f$  is the standard deviation of the fit

$$\text{residuals given by } \sigma_f = \sqrt{\frac{\sum_{q=1}^M [\alpha_{\text{exp}}(v_q) - \alpha_{\text{fit}}(v_q)]^2}{M - k}}, \text{ in which } \alpha_{\text{exp}}(v_q) \text{ and } \alpha_{\text{fit}}(v_q) \text{ are the}$$

measured and fitted frequency-dependent absorption coefficients, respectively,  $M$  is the number of spectral points, and  $k$  is the number of adjustable line shape parameters in the fit model.

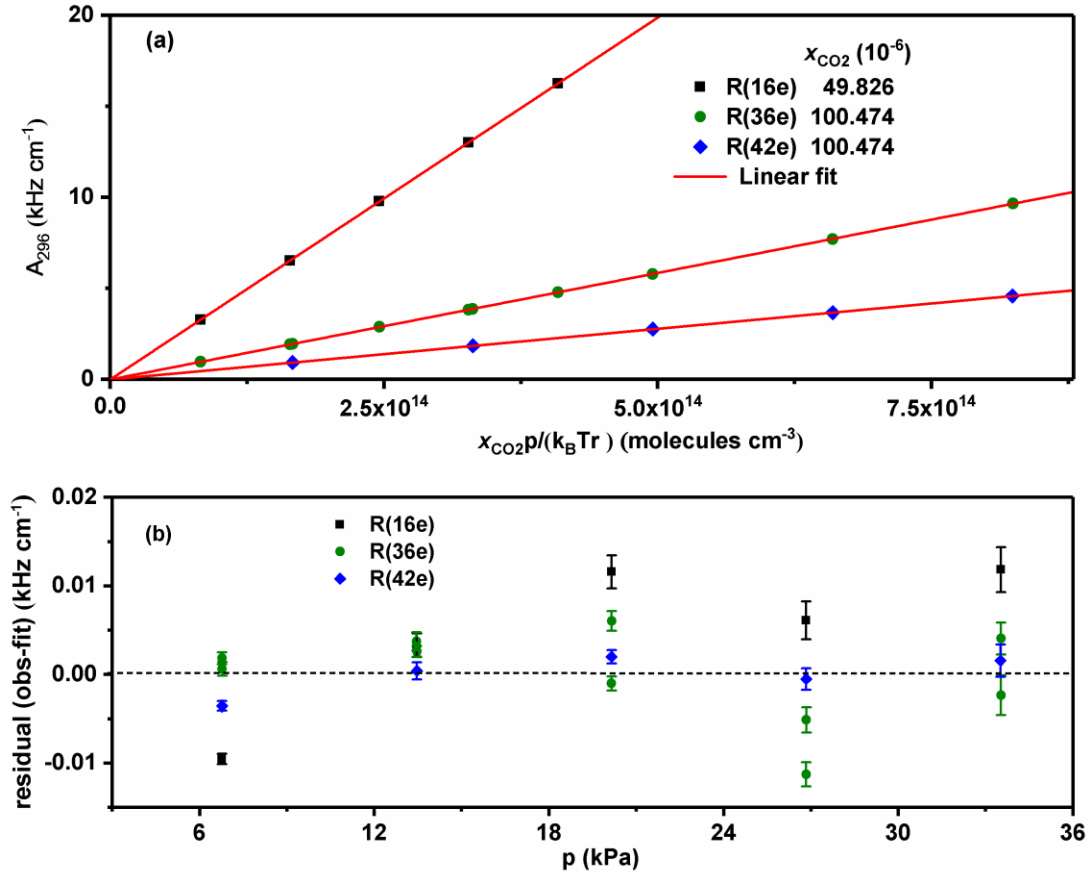


**Figure 5.** (a) Plot of temperature-corrected, fitted line areas ( $A_{296}$ ) vs. CO<sub>2</sub> number density at  $T_r = 296$  K for the R16, R36 and R42 (20012) - (00001) band  $^{12}\text{C}^{16}\text{O}_2$  transitions. Error bars correspond to the standard uncertainty of the area reported by each spectrum fit, and the lines correspond to weighted linear regressions (with constrained 0-intercept) whose slopes yield the intensities of the respective transitions. Relative uncertainties for the fitted slopes were less than 0.03 % for all three lines. (b) Residuals from the multispectral fit illustrating the high degree of linearity of the fitted peak areas.

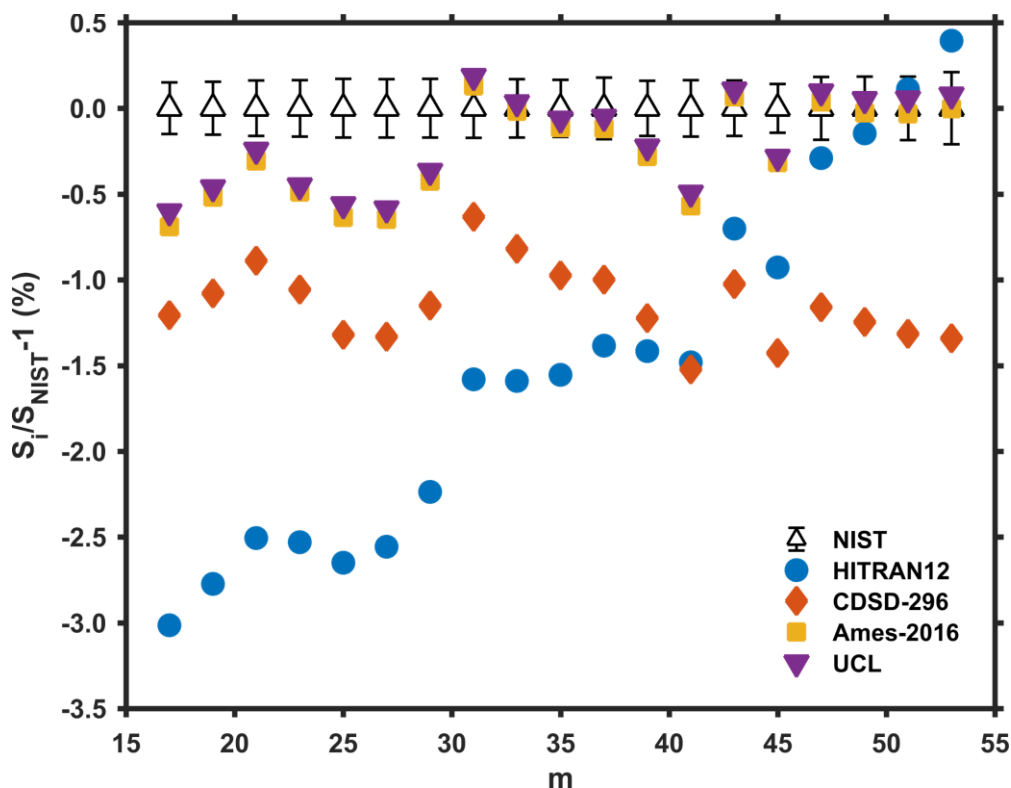


**Figure 6.** (a) Relative differences  $\varepsilon = S_i/S_{NIST} - 1$ , where  $S_{NIST}$  are the NIST transition intensities (reported herein) and  $S_i$  are the intensities from various CO<sub>2</sub> line list databases. For reference, the relative difference for the NIST intensities as compared with themselves are plotted as open black triangles with appropriate standard uncertainties. Values of  $\varepsilon$  for comparisons with HITRAN 2012 (Fourier transform laser spectroscopy), CDSD-296 (calculated effective dipole moment surface (DMS)), Ames-2016 (*ab initio* DMS), and UCL (*ab initio* DMS) are also plotted as circles, diamonds, squares, and inverted triangles, respectively. The standard uncertainties for each database (not shown) are: HITRAN 2012, 1 % [14, 25]; CDSD-296, 1.6 % [26]; Ames-2016, 1-3 % [27]; UCL, 1 % [20, 23]. While HITRAN 2012 and CDSD-296 intensities show systematic deviations from the NIST values, the UCL and Ames-2016 *ab initio* DMS intensities are in good agreement throughout the *R*-branch of the (20012) - (00001) <sup>12</sup>C<sup>16</sup>O<sub>2</sub> band.

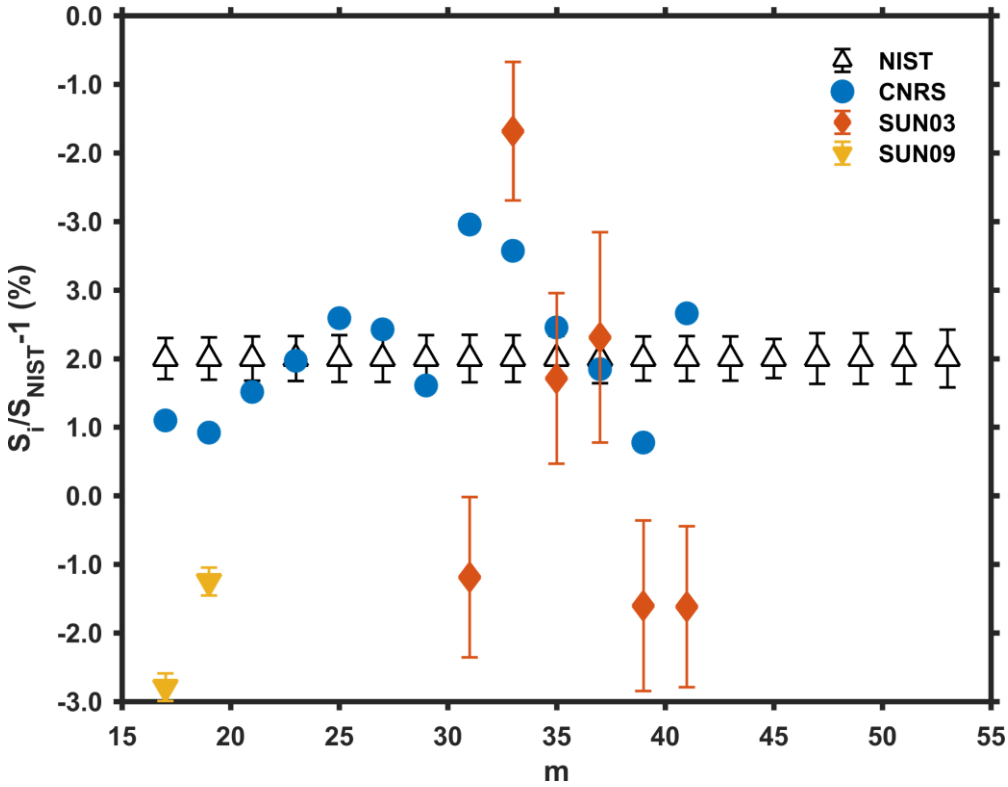


**Figure 7.** (a) Relative differences  $\varepsilon = S_i/S_{NIST} - 1$ , where  $S_{NIST}$  are the NIST transition intensities (reported herein) and  $S_i$  are the intensities from various experiments in the literature. For reference, the relative difference for the NIST intensities as compared with themselves are plotted as open black triangles with appropriate standard uncertainties. Values of  $\varepsilon$  for comparisons with CNRS [29], SUN03 [30], and SUN09 [32] are also plotted as circles, diamonds, and inverted triangles, respectively. Each experiment reported using tunable diode laser spectroscopy and/or Fourier transform infrared spectroscopy to measure (20012) - (00001)  $^{12}\text{C}^{16}\text{O}_2$  intensities [29-32]. The standard uncertainty for the CNRS data (not shown) is 2 % [29], while standard uncertainties for the SUN data set are plotted along with the reported values [30-32].

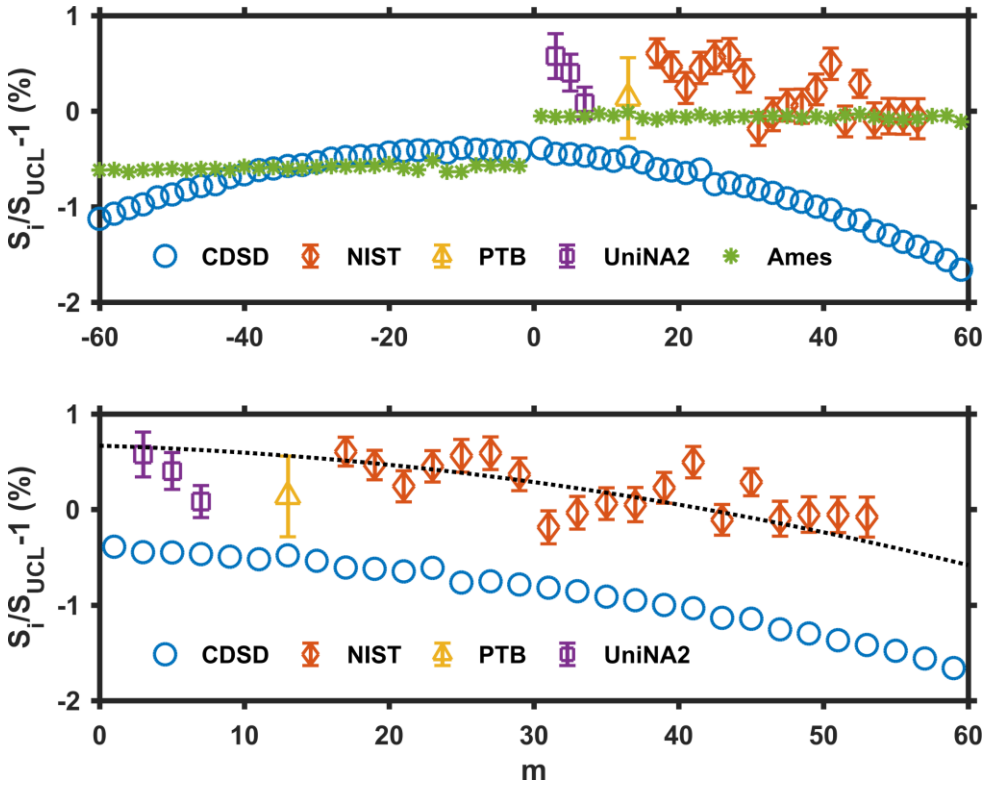


**Figure 8.** Top panel: Comparison of intensities relative to *ab initio* calculations (UCL line list) for P- and R-branches of the (20012) - (00001)  $^{12}\text{C}^{16}\text{O}_2$  band. Here,  $m = -J''$  and  $m = J'' + 1$  for the P- and R- branches, respectively. Intensities are expressed as a relative difference with respect to the corresponding UCL [20, 23] line list value,  $\epsilon_{UCL} = S_i/S_{UCL} - 1$ . Relative uncertainties for the CDS [26] data base (1.6 %) and the Ames-2016 [27] data base (1-3%) are large compared to recent high-precision measurements of NIST (reported herein), PTB [33], and UniNA2 [34], and therefore are not shown. Bottom panel: Comparison of  $\epsilon_{UCL}$  vs.  $m$  for only the R-branch of the (20012) - (00001)  $^{12}\text{C}^{16}\text{O}_2$  band. Plotted in dotted black line is a quadratic regression curve of the CDS data set fitted for  $|m| \leq 60$  and shifted by  $\delta_{\epsilon_{UCL}} = +1.1\%$ .